LIU, Z., TAKAHASHI, T., LINDSAY, D., THEVAR, T., SANGEKAR, M., WATANABE, H.K., BURNS, N., WATSON, J. and THORNTON, B. 2021. Digital in-line holography for large-volume analysis of vertical motion of microscale marine plankton and other particles. *IEEE journal of oceanic engineering* [online], 46(4), pages 1248-1260. Available from: https://doi.org/10.1109/JOE.2021.3066788

Digital in-line holography for large-volume analysis of vertical motion of microscale marine plankton and other particles.

LIU, Z., TAKAHASHI, T., LINDSAY, D., THEVAR, T., SANGEKAR, M., WATANABE, H.K., BURNS, N., WATSON, J. and THORNTON, B.

2021

Digital in-line holography for large-volume analysis of vertical motion of micro-scale marine plankton and other particles

Zonghua Liu [1], Tomoko Takahashi [2], Dhugal Lindsay [2], Thangavel Thevar [3], Mehul Sangekar [1,2], Hiromi Kayama Watanabe [2], Nicholas Burns [3], John Watson [3], Blair Thornton [1, 4]

1 *Institute of Industrial Science, University of Tokyo, Tokyo, Japan*; 2 *X-STAR, JAMSTEC, Yokosuka, Kanagawa, Japan*; 3 *School of Engineering, University of Aberdeen, Aberdeen, UK*; 4 *Centre for In Situ and Remote Intelligence, Faculty of Engineering and Physical Sciences, University of Southampton, Southampton, UK*

Abstract: Measuring the distribution, characteristics and dynamics of marine micro-scale plankton and other particulate matter is essential to understand the vertical flux of elements in the marine environment. Digital holographic microscopy is a powerful approach for measuring these and studying their 3D trajectories in a relatively large observation volume. This paper demonstrates a compact, in-line digital holographic microscope that allows large-volume and high-resolution recording of marine particles through combining a continuous wave laser and a short exposure CMOS camera with efficient global shutters. A resolution of better than 10 μm is demonstrated in air and the minimum distinguishable size of targets recorded in water is approximately 20 μm. The maximum volumetric throughput of the setup is 1904 mL/s. The microscope can take motion blur free holograms of particles moving at up to 490 mm/s in theory, and has been tested in the ~200 mm/s flowing water. The orientation of the measured volume improves the ability of digital holography in profiling sinking rates and active vertical migration. The system was tested onboard a research vessel to record a range of live plankton and other particles. The motion of some samples, including the sinking motion and swimming motion, was analysed using custom developed image processing software. The experimental results show that the combination of high resolution and a large volume over which motion of sparse-distribution particles can be tracked, can improve the ability to differentiate between different types of marine particle and identify behaviours of live plankton.

Key words: digital in-line holographic microscopy, large-volume recording, marine plankton and particle motion tracking, vertical profiling of particulates, holographic image processing

1 Introduction

Micro-scale marine plankton and other particles play a key role in the vertical transport of carbon, nitrogen, phosphorus, oxygen and other elements in the ocean. Their occurrence, variety and distribution are indicators of marine ecosystem health and function [1],[2]. Active particles, such as live plankton, use energy available in the environment to drive and trigger different motion patterns. Monitoring these behaviours is important to understand their ecological and evolutionary strategies [3],[4]. Global scale analysis of movements of marine particles is also vital to model the transport of carbon and energy between organisms living near the surface and the deep sea. Examples of trends in vertical matter transport [5] that need to be understood include ingestion, fragmentation and sinking of faecal and other material [6],[7], as well as behaviours such as predation [8], escape [9] and swimming [10]. However, due to the technical difficulty of monitoring the sparse distribution of particles in the deep sea, the majority of such research has been focused on the upper ocean (shallower than 200 m) and our understanding of these processes in the deep sea is limited [5],[6].

The traditional way to study micro-scale particles in the deep ocean is to recover samples using fine-meshed nets and filters, and use an objective microscope to observe and analyse them in a laboratory. However, reliance on ships to deploy equipment and offline analysis after the recovering of sampling devices (*e.g.* microscopes) limit the spatial and temporal resolution and extent of monitoring possible, due to the high cost and limited availability of crewed research vessels. Methods (*e.g.* Benthic Underwater Microscope [11]) for *in situ* observations also exist. However, the narrow depth of field makes standard objective microscopes unsuitable when large-volume observation is necessary, as particle abundances are several orders-of-magnitude lower in the deep open ocean than in shallow areas, making their distribution sparse and much harder to detect [5].

Optical imaging techniques such as shadowgraph [12] and fluorography [13], on the other hand, allow large numbers of particles to be visualised in real time. These approaches are useful for analysing particles in bulk, but they lack the ability to measure their 3D movement. However, to understand ecological functions and their mechanisms, it is important to track the motion of particles with sufficient resolution, and this is also helpful to identify what type of particles they are [7]. Holographic imaging benefits from a much longer field depth relative to image resolution than other optical techniques [14],[15]. Digital holographic microscopy (DHM) has been used to study the 3D motion of marine particles and organisms [8]-[10],[16],[17], investigating response to controlled stimuli of targets that have been physically constrained in laboratory conditions. To study the distribution of unconstrained plankton and other particles, ocean deployable *in situ* holographic microscopes such as Holosub [18], [19], eHoloCam [20], HoloSea [21] and LISST-Holo2 [22] have been developed (see TABLE 2). However, large volumetric throughput (*e.g.* Holosub and eHoloCam) holographic devices for studying deep-sea particles typically use pulsed lasers that are large and power-hungry, which makes them unsuitable for long-term recording in deep water.

The aim of this paper is to investigate a method to track the 3D motion of micro-scale particles at a resolution high-enough (~20 μm) to identify their type from their morphology, and over a volume that is large enough (~12 mL) to identify sparsely distributed particles and gather reliable measurements of their vertical motion. To achieve this, we demonstrate the combination of a continuous wave (CW) laser and a fast CMOS sensor with low parasitic gain to achieve high resolution and motion blur free holograms of marine particles. This compact, low power instrument can achieve up to 1904 mL/s volumetric throughput, which is on the scale needed for monitoring of deep-sea particulate matter. The method is demonstrated using an experimental setup to measure the vertical/3D motion of living/non-living particles in seawater.

2 Measurement System

A lensless, in-line DHM is developed with the capability of recording micrometre-order spatial features of marine particles, such as micro- and meso- plankton (20 – 2000 μm [23]). A CW laser is used as the light source. An alternative is to use pulsed lasers to capture motion blur free images of moving objects. However, pulsed lasers are typically more expensive, larger and less robust to failure than conventional CW lasers due to the larger number of photoelectric components and increased risk of optical damage. In order to achieve motion blur free images using a CW laser, we use a CMOS camera with a short exposure time. While the microsecond-order exposure time achieved by using CMOS cameras is still several orders of magnitude longer than a nanosecond pulsed laser, it is not an issue to record motion blur free images using a sensor with a ~5 μm resolution and ~10 μs exposure time when imaging targets that laterally move with a relative speed of less than 500 mm/s (5 μm / 10 μs). The 10 μs exposure is low enough to record active marine particles, such as plankton, with mean *in situ* swimming speeds ranging from about 10 to 90 mm/s [24] (see TABLE 1 for some species). The efficient global shutter [25] with a low parasitic light sensitivity in the camera also facilitates capturing the shape of fast-moving targets.

TABLE 1. MOTION SPEEDS OF SOME MARINE PLANKTON

Marine Plankton	Average Motion Speed (mm/s)
Acartia tonsa nauplii [9]	escape swimming: 15.0 – 29.5
Temora longicornis adults [26]	swimming: 2 – 10
Temora longicornis nauplii [27]	swimming: 0.03 – 1.23
Heterosigma akashiwo [28]	swimming: ~0.5
Prorocentrum minimum [10]	swimming: ~0.1

In order to improve the functionality of DHM for measuring a large range of motion in the vertical direction, the measurement channel is designed to be upright and the system appearance looks like a real microscope. Another reason for this design is that the system is expected to be mounted on some ocean platforms in the future, such as Argo floats and gliders. Considering mountable compatibility with other devices, the system cannot be designed to be too long. Besides this, the high-resolution recording requirement also restricts the body length of the system [15].

2.1 Optics Design

The optical components are arranged to make inline measurements of a vertically oriented channel as illustrated in Fig. 1. The setup consists of two main housings: a flow tube and a waterproof hull. The length of the measurement channel in the flow tube is 200 mm, with an internal diameter of 16 mm. A compact 785 nm wavelength single mode CW laser (Oxxius LBX-785S-150-ISO-PPF, 40 × 40 × 100 mm) is used as the light source. Near infrared light was chosen because plankton tends to exhibit low sensitivity to this wavelength [29],[30]. The laser is coupled to a single mode fibre (Thorlabs P3-780AR-2), and light coming out of the fibre is collimated in a waterproof housing. This collimated 12 mm diameter beam passes through a sapphire window (Thorlabs WG31050) to illuminate particles suspended in the measurement channel. The light passes through the second sapphire window (Thorlabs WG31050) and an attenuation filter (OptoSigma AND-25C-20) before being recorded by a

CMOS detector (JAI GO-5100-USB, 29 × 29 × 41.5 mm). The detector has a resolution of 2464 × 2056 with a pixel pitch of 3.45 × 3.45 μm (Binning 1 mode), giving an active area of 8.5 mm × 7.09 mm. The volume observed in each frame using this setup is 12 mL (8.5 mm × 7.09 mm × 200 mm), where the maximum frame rate at the 3.45 μm resolution is 74 fps, giving a theoretical maximum volumetric throughput of 892 mL/s. It can work in another mode (Binning 2) where a square of four adjacent pixels is binned as one pixel. In this mode, the pixel pitch becomes 6.90 μm × 6.90 μm, and the frame rate can reach 158 fps, which improves the maximum volumetric throughput to 1904 mL/s. The flow through the tube can be controlled by connecting a pump at the outlet valve.

The detector has a short exposure time of 7 μs with low parasitic exposure (< 0.002%) when the electronic shutter is closed, allowing high-resolution motion blur free capture of objects moving at up to 490 mm/s (3.45 μm / 7 μs, please see details in Section 3.2) in theory, which is sufficient to record the 3D motion of many active marine particles. This movement tolerance will also enable the proposed system to be mounted on Argo floats and gliders (Argo floats – ~100 mm/s, gliders – ~350 mm/s) in future.

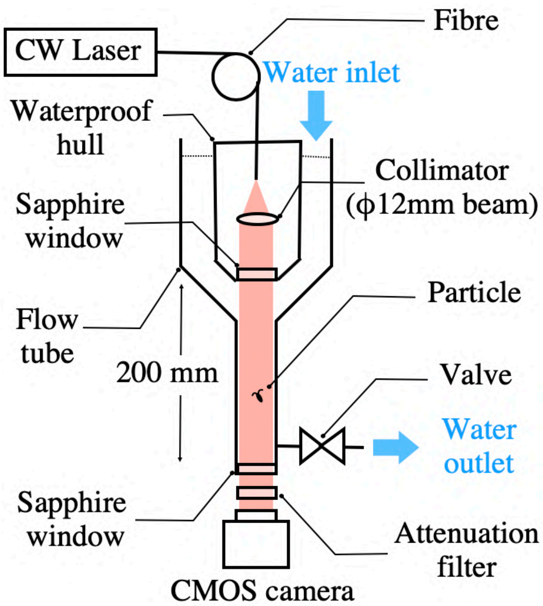

Fig. 1. Schematic of the in-line holographic microscope.

TABLE 2 shows the specification of six representative holographic imaging systems and the system developed in this work. The nanosecond pulsed lasers adopted in Holosub, eHoloCam and HoloSea allow measurements of particles that move several orders of magnitude faster than CW laser systems. However, this is significantly faster than the speed of the particles targeted in this work. Like Holosub and eHoloCam, the large volumetric throughput makes the proposed setup more suitable for measuring sparsely distributed plankton and particles than other instruments which also use a CW laser.

TABLE 2. SPECIFICATIONS OF SIX REPRESENTATIVE SYSTEMS AND THAT DEVELOPED IN THIS PAPER

System	Size (diameter × length: mm^2)	Laser Mode	Minimum Pixel Pitch (µm)	Maximum Movement Tolerance * (mm/s)	Maximum Frame Rate (fps)	Sampling Volume Per Hologram (mL)	Maximum Volumetric Throughput (mL/s)
Holosub [18]	/ **	pulsed (50 ns)	7.4	1.48×10^5	14.7	40.5	595
eHoloCam [20]	330 × 1350	pulsed (5 ns)	3.5	7×10^5	25 ***	36.5	~920
HoloSea [21]	92 × 351	pulsed (500 ns)	~2.0	$\sim 4.1 \times 10^3$	22	~0.3	~6.6
LISST-Holo2 [22]	133 × 767	continuous	4.4	/	25	~2	45.6
Submersible Holographic Particle Imager [31]	~100 × 630	continuous	7.4	740	25	~1.7	~42.5
DIHM in [32]	~150 × 890	continuous	7.4	118	7	1.8	12.6
Our System	~158 × 502	continuous	3.45	490	158 ****	12	1904

* This specification is calculated by dividing the shortest exposure time by the minimum pixel pitch.
** / indicates there is no information found about this specification.
*** at pixel pitch of 10.5 µm
**** at pixel pitch of 6.90 µm

2.2 Data Processing

The data processing in this work extracts the 3D position of particles in the imaging volume from reconstructed holograms. The angular spectrum method [33] is used to reconstruct holograms in this study. The depth positional information of an object is obtained using the focus metric of absolute Tenengrad [34], shown in Eq. (1):

$$T_{grad} = \sum_{i,j}(|f(i,j) \otimes S| + |f(i,j) \otimes S'|), \quad (1)$$

where $f(i,j)$ signifies an image and $\otimes$ indicates convolution; S and S' are the two Sobel kernels with $S = [1\ 0 - 1;\ 2\ 0 - 2;\ 1\ 0 - 1]$. In order to improve its performance, a weight is given to each gradient value by multiplying the edges detected using structured forests [35]. Eq. (1) now becomes:

$$T_{grad} = \sum_{i,j}(|f(i,j) \otimes S| + |f(i,j) \otimes S'|) \cdot e(i,j), \quad (2)$$

where, $e(i,j)$ is the edge image.

Fig. 2 shows the focusing performance of the two metrics on two holograms. These two images show that the weighted absolute Tenengrad outperforms the normal Tenengrad when they are used to automatically look for the focused reconstructing distance for a hologram. Each hologram is processed with 1000 reconstructing slices at 0.2 mm range intervals.

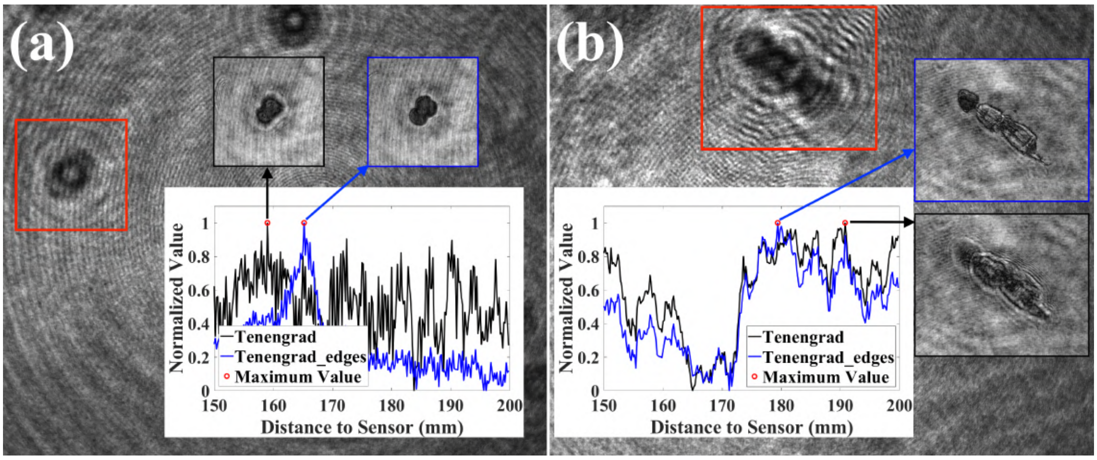

Fig. 2. Performance of two focus metrics on two holograms. The plotting figures show the Tenengrad values (normalised in the range from 0 to 1) of the outlined regions (in the red boxes) that are calculated in a distance range from 150 mm to 200 mm. The focused reconstructions of the region based on the two metrics are also displayed on each hologram.

To determine the (x, y) plane position of the target in the focused reconstruction, the target particle is segmented using a convex hull tool that is constrained by manually identified dominant points on its outline (see Fig. 3). The centroid of the segment is calculated and converted from the image frame to the spatial frame. Combining this with the focus distance gives the 3D coordinate of the centre of each object.

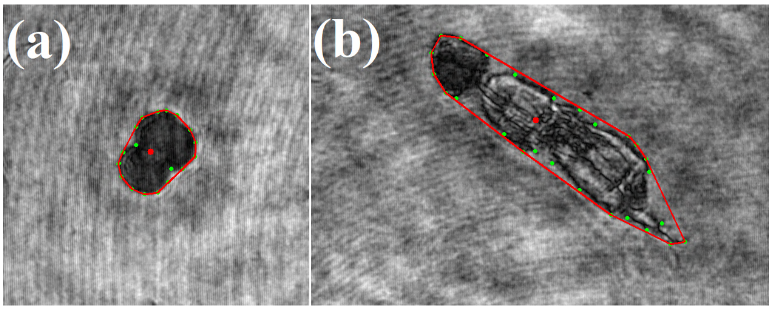

Fig. 3. Two examples showing the drawn convex hull (red line) based on the selected dominant points (green points) and object centres (red point) whose 3D coordinates are (298, 766, 165.2) and (1056, 290, 179.4) respectively. These two images are cropped from their focused reconstructions after auto-focusing. The (x, y) position is calculated based on the full image dimension.

3 System Performance Analysis

3.1 Resolution Estimation

Resolution in DHM depends on some parameters of the setup [16], such as the laser wavelength, and the size and recording position of the sensor. It includes the lateral resolution (in the x-y plane) and longitudinal resolution (along z direction). The resolution of a digital holographic camera can be estimated theoretically and experimentally. The calculation of resolution in theory is normally based on the Rayleigh and Sparrow criteria [36], and the experimental estimation is usually implemented using a resolution target.

3.1.1 Longitudinal Resolution and Reconstructing Interval

The longitudinal resolution can be defined as the minimum distance between two discrete point targets along the optical axis that can be resolved in the recorded image. This resolution in DHM is difficult to directly measure, especially in the in-line setup [16]. However, it is necessary to know this parameter because it determines the minimum interval in direction z during reconstructing a hologram. It is suggested that this resolution can be indirectly estimated through computing the quality of reconstructions at different reconstructing distances [37].

Eq. (2) is used during indirectly estimating the longitudinal resolution of the instrument in this work. The procedure is: for a hologram, first use Eq. (2) to compute T_{grad} of its focused reconstruction at distance d_{focus} (this focused reconstruction is obtained from the auto-focusing algorithm described in Section 2.2); and this equation is also used to compute T_{grad} in a reconstruction reconstructed at a given distance d; the difference of these two reconstructions is then computed based on the equation below.

$$Difference\ (d) = \frac{|T_{grad}(d) - T_{grad}(d_{focus})|}{T_{grad}(d_{focus})}. \quad (3)$$

This equation above is used to calculate the difference between the focused reconstruction and out-of-focus reconstructions of the regions of interest in the two holograms in Fig. 2. Their focused reconstructions are shown in Fig. 3. For the region in (a), its focus distance is 165.4 mm, and the estimation distance range is from 155 mm to 175 mm; for region (b), its focus distance is 179.4 mm, and the estimation distance range is from 170 mm to 190 mm. The reconstructing interval is 0.01 mm.

Fig. 4 shows the results from the two regions. Since much noise exits, two curves fluctuate sharply. However, it can still be observed that the values quickly decrease beside the focuses in the two curves. This indicates that unfocused reconstructions reconstructed at distances close to the focus become significantly similar with the focused reconstruction (< ~5% in difference) and they become undistinguishable. Therefore, if the threshold of difference is set as 5%, the longitudinal resolution of the setup can be speculated to be around 0.2 mm based on the measure of Eq. (3).

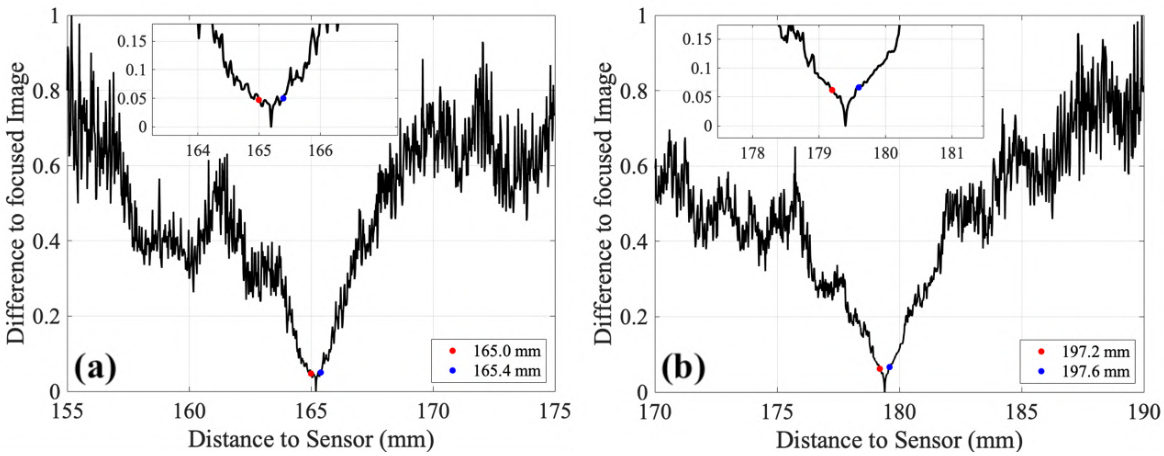

Fig. 4. Two examples showing the difference between the focused image and unfocused images. (a) shows the difference values calculated on region (a) in Fig. 3, and (b) shows the values on region (b) in Fig. 3. The magnified figures show the detail of the peaks. The peaks are located at their focus distances respectively (165.2 mm and 179.4 mm). The red and blue spots are localised at -0.2 mm and +0.2 mm from the focus respectively.

Theoretically, it should be better if the reconstructing interval is defined as smaller as possible. However, that will make the reconstructing procedure too time-intensive. The reconstructing interval in practice should be decided by the longitudinal resolution. Since the exact longitudinal resolution of DHM is difficult to achieve, the interval can be decided by the speculated value based on the given measure and it is defined as 0.2 mm in this paper.

Another factor that affects the reconstructing interval is the target size, and the interval should be smaller when reconstructing holograms of smaller targets. The sizes of the main objects observed in this paper are in the range of several hundreds of micrometres to several millimetres. Fig. 5 shows several reconstructions of the two regions in Fig. 3 around their focus distances. The sizes of the objects are around 500 μm (in the top row) and 2 mm (in the bottom row). For each object, it can be observed that reconstructions of within 0.2 mm from its focus are visually same with the focused reconstruction ((a-3) and (b-3) respectively). Therefore, the reconstructing interval of 0.2 mm is reliable during reconstructing holograms in this work.

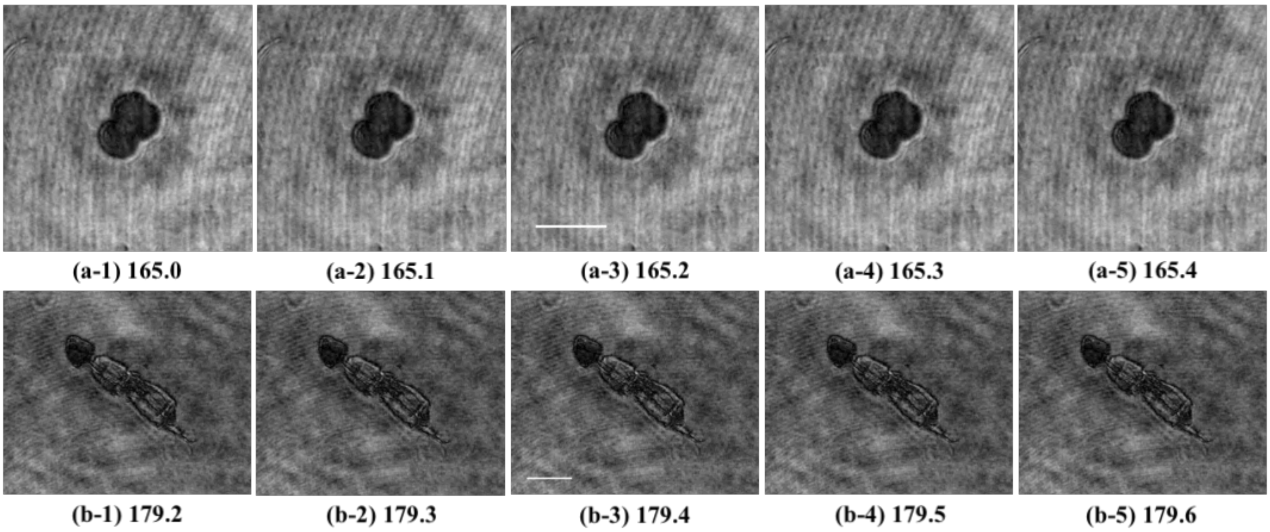

Fig. 5. Reconstructions of two regions in Fig. 3 at several different distances. Their focus distances are 165.2 mm (a-3) and 179.4 mm (b-3) respectively. The scales indicate 500 μm in (a-3) and (b-3).

3.1.2 Lateral Resolution

In air: The theoretical lateral resolution of a reconstructed in-line hologram in air, r, can be approximately calculated using Eq. (4) [15], [16]:

$$r = \frac{\lambda}{D} d, \quad (4)$$

where λ is the laser wavelength, D is the diameter of the holographic image (normally simplified to the image diagonal length), and d indicates the distance of the image plane to the sensor plane. The resolution that is achieved is dependent on the distance of the image plane from the sensor plane due to the diffraction limit as shown in Fig. 6 (black line). The actual lateral resolution can be measured using a resolution target. Fig. 6 shows the experimentally derived lateral resolution of our setup that was measured using a resolution target (ThorLabs NBS1963A) in air. Measurements were carried out for an image plane distance of 70 to 270 mm at an interval of 20 mm.

The pixel pitch of the detector also limits the achievable resolution. This is shown in Fig. 6, where the resolution of the nominal 3.45 μm pixel pitch of our detector is shown in red (Binning 1), and the resolution for double binning (Binning 2), where 4 pixels are binned together with an effective pitch of 6.90 μm shown in blue. Beyond 180 mm range, the two modes are almost identical since the lateral resolution is diffraction limited. However, when the image plane is closer than 180 mm the smaller pixel pitch in the nominal mode has a higher resolution, achieving a maximum of 8.8 μm at 70 mm range.

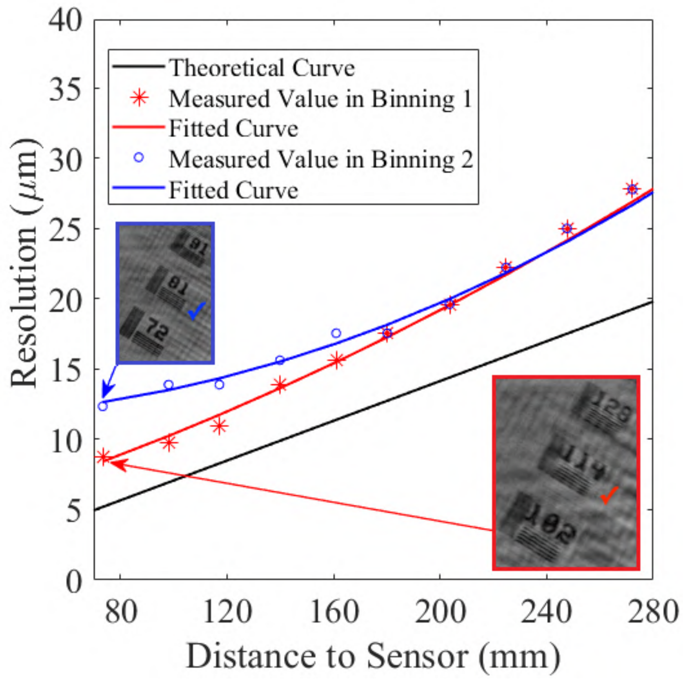

Fig. 6. Lateral resolution of the system in theory (black line) and measured experimentally. The experiment for the pixel pitch of 3.45 μm (Binning 1) is in red, and Binning 2, which has an effective pixel pitch of 6.9 μm is shown in blue. The two images show the best resolution in the two modes, where Binning 1 can resolve 114 lines per mm, and Binning 2 can resolve 81 lines per mm, corresponding to lateral resolutions of 8.8 and 12.3 μm respectively (at 70 mm distance to sensor). The fitted curves are generated using the method of polynomial curve fitting.

In water: Since the flow channel is narrow (16 mm diameter), it is difficult to place the resolution target in the channel to measure the actual lateral resolution of the system in water. This parameter is estimated by the size of the minimum visible particles recorded by the system. Fig. 7 shows two particles at the scale of 20 μm recorded when the pixel pitch is 3.45 μm. Their basic shape features are discernible. Therefore, we speculate that the system at best could be able to discriminate particles with the scale of 20 μm at this resolution.

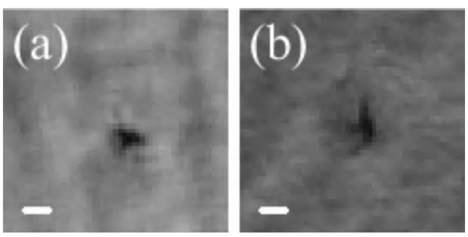

Fig. 7. Two particles recorded at the distance of 70 mm when the pixel pitch is 3.45 μm. The scales indicate 20 μm.

3.2 Motion Blur Estimation

Motion blur is caused by target moving with respect to the camera during the period of exposure time. It is determined by the object moving speed, and camera exposure time and viewpoint towards the target [38]. A simple equation [39] used to calculate motion blur of a moving target is:

$$Blur_{motion} = \upsilon t_e, \quad (5)$$

where, υ is the object moving speed and t_e is the camera exposure time.

Theoretically speaking, if the motion blur projected to the sensor plane is less than a pixel length, this blur cannot happen in a digital image. The camera pixel size in our system is 3.45 × 3.45 µm. Therefore, based on Eq. (5), as long as the target moves at a speed less than 490 mm/s (3.45 µm / 7 µs), the camera should be able to capture its moving without motion blur.

Since it is nearly impossible to exactly control the moving speed and direction of an object towards to the sensor in water, it is difficult to provide an experimental test of the maximum movement speed. However, we recorded many holograms of lifeless organic samples in flowing water with different speeds (*e.g.* dead plankton, the active moving can be avoided using dead samples such that the flow speeds can roughly be regarded as the moving speeds of the samples). The maximum flow speed tested was around 200 mm/s. The exposure time of the camera was 7 µs and the pixel pitch size is 3.45 × 3.45 µm. Some examples are shown in TABLE 3. The reconstructed holograms recorded in flowing water look similar with the reconstructed holograms recorded in the still water, and no motion blur can visually be observed on them. This indirectly shows that the setup is able to record clear holograms of moving particles with a speed of around 200 mm/s at least. This speed tolerance has actually been high enough to record most of moving plankton in oceans.

TABLE 3. HOLOGRAMS RECORDED IN STILL WATER AND FLOWING WATER WITH DIFFERENT SPEEDS

Flow Speed (mm/s)	Sample1	Sample2
0.0	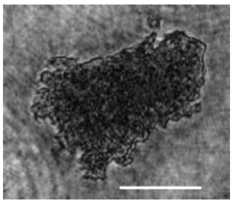	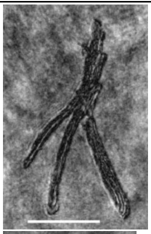
~ 153.9	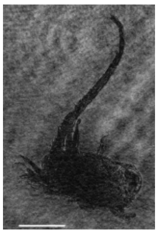	
~ 175.2	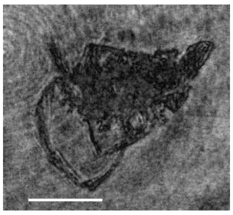	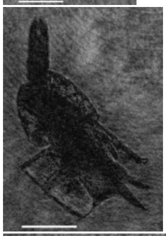
~ 196.4	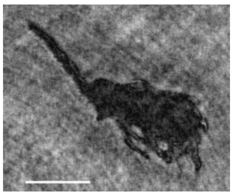	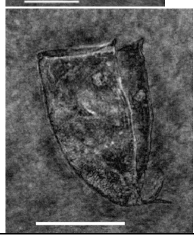

Note: The scales indicate 500 µm.

4 Experimental Results

Some experimental results are shown in this section. In the experiments below, the camera exposure time was set as 7 µs and the frame rate was 10 fps. The beam intensity after the collimator was about 11 mW, and it became ~2 mW after the beam passed through the attenuation filter (transmissivity – 20%) when there was no water in the measurement chamber.

The image processing methods used to process holograms have been described in Section 2.2, including the algorithms of auto-focusing and object position extraction.

4.1 Recording Marine Plankton

The measurement system was used to record and study plankton and other particles during a cruise of the R/V *Yokosuka* (YK20-E02) conducted in February 2020 in Sagami Bay and Suruga Bay, Japan. Fig. 8 shows some plankton recorded during the cruise. These were collected from a large range from deep sea to upper ocean using a net mounted on a Deep Tow camera system [40] and observed onboard the ship soon after being recovered on deck. The measured plankton included a copepod larvae in (a and b), larvaceans in (c) and (f), a jelly in (d), a copepod nauplius larva in (e), a euphausiid furcilia larva in (g), copepods in (h, i, j and k), and a chaetognath in (l). Their sizes range from a few hundred microns (a, b) to several millimetres (k and l).

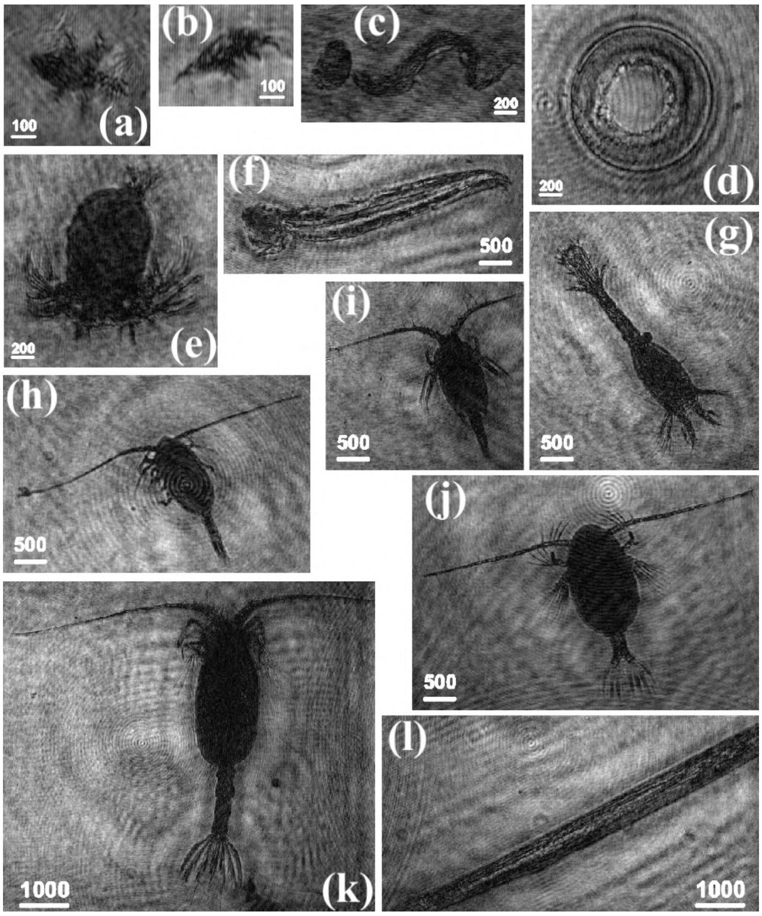

Fig. 8. Plankton recorded during the cruise. The unit of scale in the images is µm.

4.2 Tracking Trajectories of Marine Plankton and other Particles

4.2.1 Sinking Motion

The vertical motion of a trachymedusan jellyfish (see Fig. 9 (a)) was measured in sea water. The holograms were reconstructed to obtain the distances to the sensor plane at different time points. Fig. 9 (b) shows one of the reconstructed holograms.

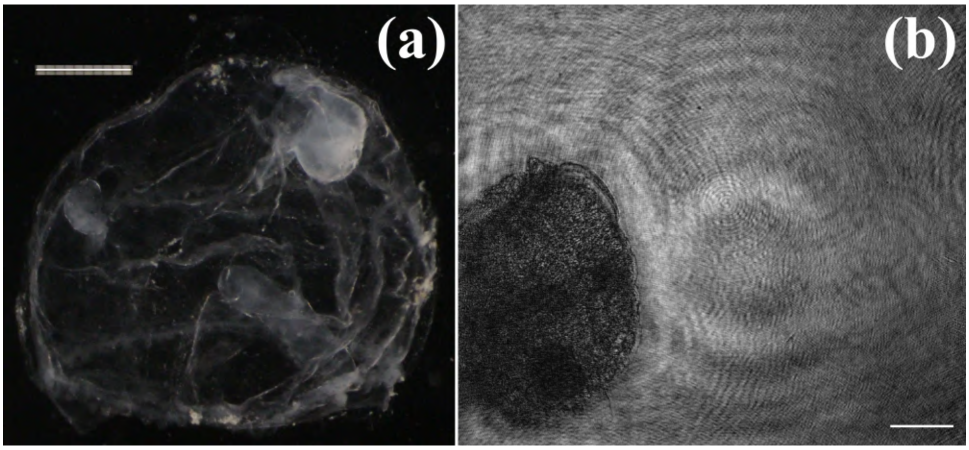

Fig. 9. Microscopic photograph of the jellyfish sample (a) and one of its reconstructed holograms (b). The scales indicate 1000 μm.

Fig. 10 shows the distances and sinking speeds of the jelly over a 20 s period, where the speed is determined by taking the derivative of the distance to the sensor. The sample sank from 256.0 mm to 168.2 mm in 20 s. The average sinking speed was 4.48 mm/s, with the particle accelerating downwards at a rate of 0.04 mm/s^2 during this period.

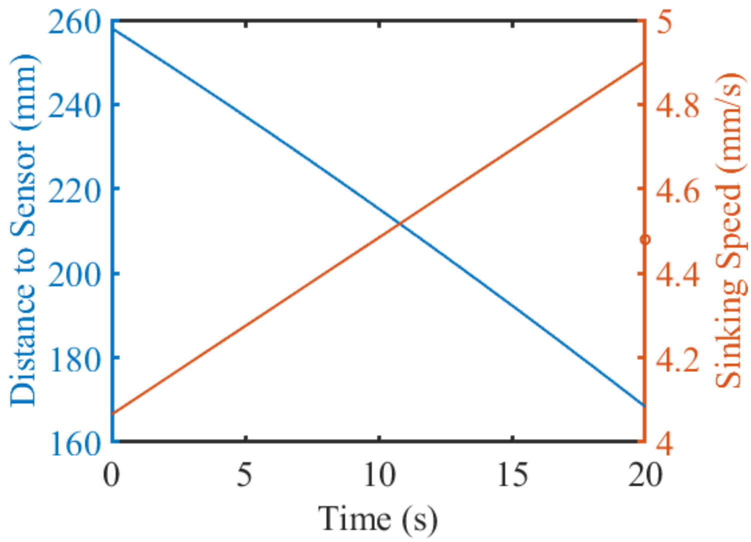

Fig. 10. Distances (blue) between the jelly sample and the sensor and its sinking speeds (brown) at different time points. The open circle on the right y-axis indicates the average sinking speed. The curves are fitted using the method of polynomial curve fitting.

We also measured the sinking speeds of some dried foraminifera particles (their main component is $CaCO_3$) in water. Fig. 11 (a) shows a photograph of them and images (b)-(g) show the reconstructed holograms of six of these particles. These six particle samples were recorded one by one. Unlike living organisms, these inorganic particles cannot actively move at all. Their density is normally greater than jellies and they tend to sink faster (see TABLE 4). The sinking speed has a relationship with the density and volume. However, the motion of particles in water is a complex phenomenon and a detailed description is not the focus of this paper. Fig. 12 depicts the sinking speeds of the six samples in the distance range of 150 mm to 200 mm from the sensor and TABLE 4 lists the average speeds of them during sinking. These data show that bigger particles tend to sink faster. It can also be observed that the sinking speeds of these particles decreased with transit time, while the jelly's speed increased as shown as in Fig. 10.

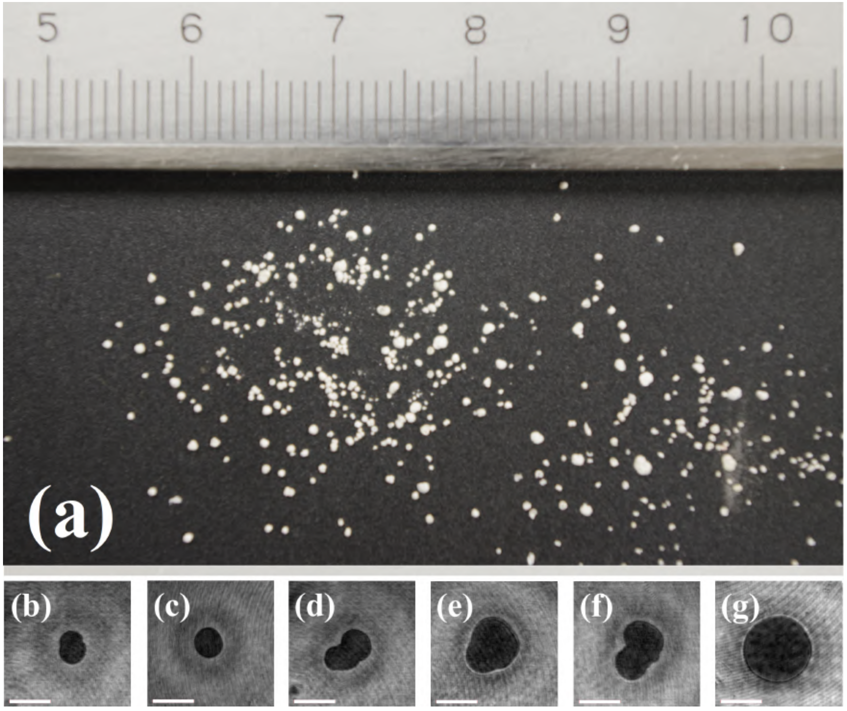

Fig. 11. Photograph of dried foraminifera particles (a) and reconstructed holographic images of six samples: (b) – Fora1; (c) – Fora2; (d) – Fora3; (e) – Fora4; (f) – Fora5; (g) – Fora6. The unit of the scale in (a) is mm. The scales in (b)-(g) indicate 500 μm.

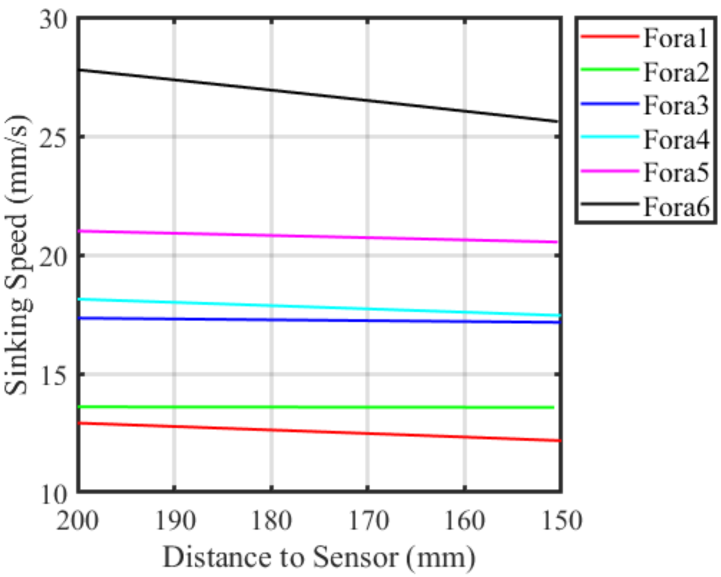

Fig. 12. Sinking speeds of six foraminifera particles at different distances to the sensor. The curves are generated using the method of polynomial curve fitting.

TABLE 4. AVERAGE SINKING SPEEDS OF THE JELLY AND SIX FORAMINIFERA PARTICLES

Sample	Jelly	Fora1	Fora2	Fora3	Fora4	Fora5	Fora6
Average Sinking Speed (mm/s)	4.48	12.55	13.59	17.24	17.79	20.76	26.66

4.2.2 Swimming Motion

The 3D swimming trajectory of a live calanoid copepod (as shown in Fig. 13 (a)) was measured in seawater. Fig. 13 (b) and (c) are two reconstructed holograms of the sample. The (x, y) position of the copepod in each image was determined as described in Section 2.2. Their body outlines and the centre coordinates in 3D are shown in (b) and (c). It should be noted that the projected shape of the copepod changes significantly during swimming behaviours and this limits the accuracy of the motion tracking and velocity measurements made by the system.

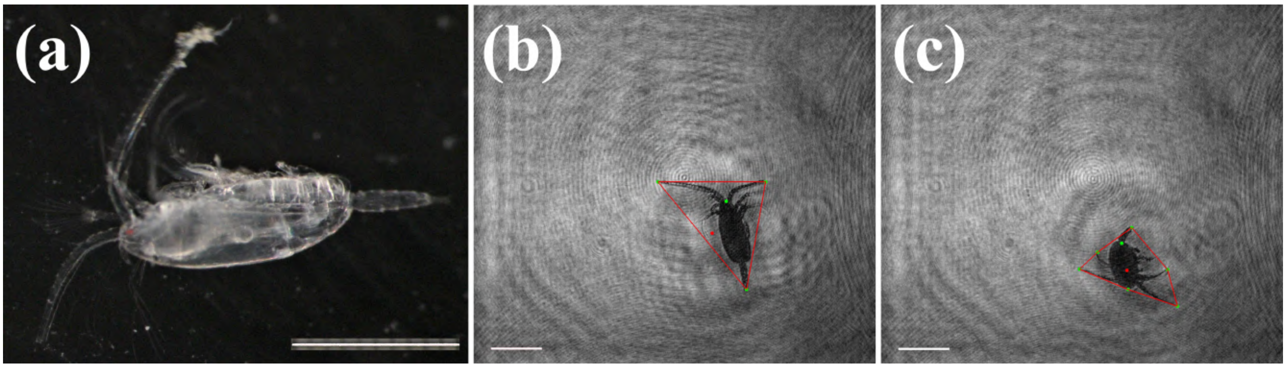

Fig. 13. Microscopic photograph of the copepod sample (a) and two reconstructed holograms (b) and (c). The red convex hulls describe the body outline in the current moment and the red spots show its 3D coordinates that are (1360, 1301, 211.6) and (1402, 1512, 216.0) respectively. The (x, y) position is calculated based on the sensor dimensions. The scales indicate 1000 µm.

Fig. 14 shows the 3D trajectory of the free-swimming copepod over 14 s. The red spots indicate the copepod positions at intervals of 0.2 s, and the arrows indicate its swimming directions. The tracked trajectory started at P1 (x = 3.91, y = 0.49, z = 231.0 mm) where the origin was measured at the top left point of the CMOS detector. The red points initially stay close to each other, showing that the copepod moved slowly laterally. The copepod then turned clockwise at 6 s (at P30) and accelerated sharply between P33 and P34 reaching 18.97 mm/s. It then turned back and moved laterally again, changing direction again at 9.2 s (P46). The winding trajectory with different colours describes that the sample slowly sank, it swam up when sensing it had been sinking, and it would sink again. The copepod gradually sank during the entire period on average, but propelled itself upwards at some points in time. The total distance travelled was 63 mm in 14 s, with an average swimming speed of 4.50 mm/s.

Fig. 15 shows the reconstructed holograms of the copepod at five time points (P30, P33, P34, P35 and P46 in Fig. 14). It can be observed that the copepod tended to turn its body over to change its swimming direction, as shown in (a), (c) and (e). It kept its body flat and folded its legs when it moved in a high speed, as shown in (b) and (d).

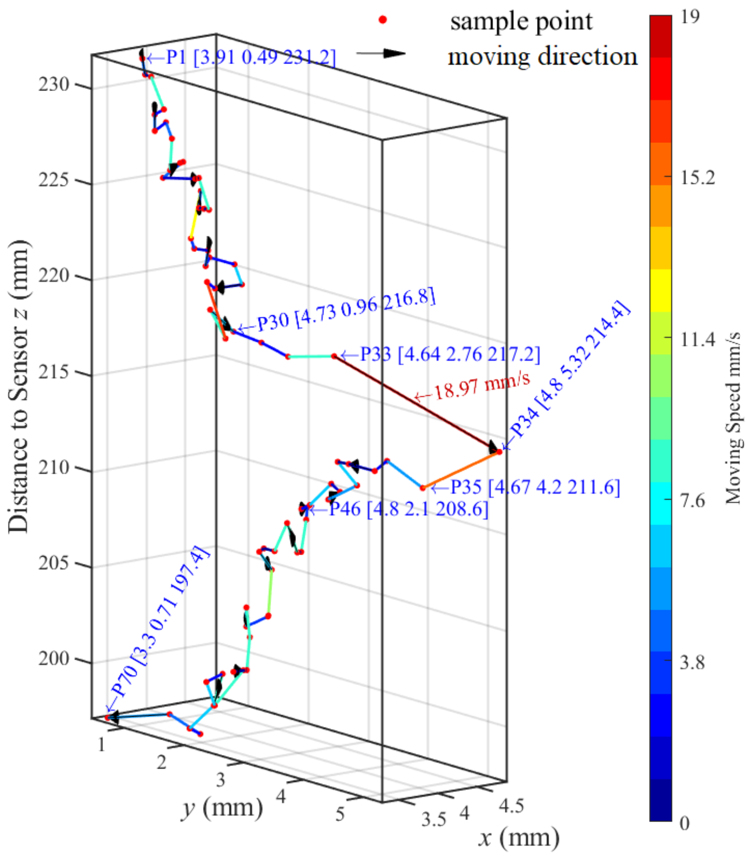

Fig. 14. 3D swimming motion of the copepod. The red dots correspond to its positions sampled every 0.2 s. The arrows indicate its swimming directions. The coordinates in blue show some sampling points. The colormap describes the average speed between two sampled points.

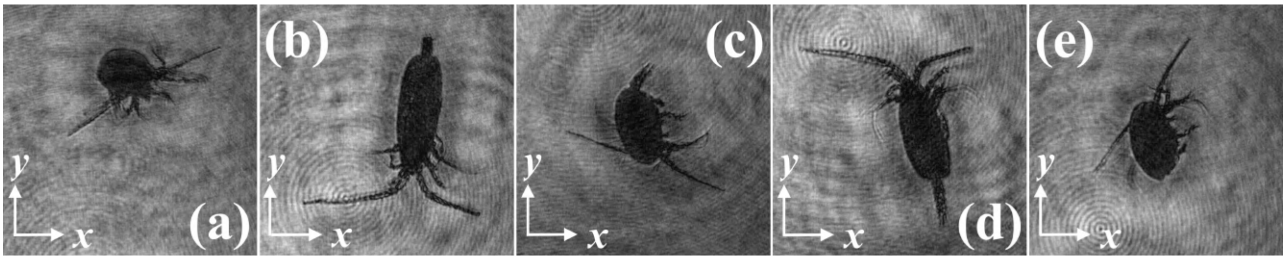

Fig. 15. Reconstructed holograms of the copepod at five time points. (a) – P30, (b) – P33, (c) – P34, (d) – P35, (e) – P46. The x and y axes have the same direction with the axes in Fig. 14.

4.2.2 Moving Speed *vs* Shape in Copepods

The high-resolution of the measurement system means that it is possible to resolve the shape of the copepod during different motion manoeuvres and investigate how the size of the target correlates with the swimming motion. The trajectories of six copepods with different sizes were tracked in Fig. 16, which shows their reconstructed holograms. The size of each copepod can be estimated from the reconstructed image.

Fig. 17 (a) shows their sinking speeds which reflect the typical motion of copepods where they slowly sink with fluctuating speeds. The vertical speed of the two smallest copepods, Cop1 and Cop2, fluctuated more widely along the z axis than the other targets. Big copepods tended to have high average sinking speeds (*e.g.* Cop5 and Cop6 in TABLE 5.) Generally speaking, copepods sink more slowly than smaller moribund jellyfish and foraminifera particles (see TABLE 4 and TABLE 5) owing to their active moving with the aid of antennae and legs. Images (b)-(g) show the moving trajectories and the instantaneous moving speeds of samples in the (x, y) plane. TABLE 5 also gives their average moving speeds in the (x, y) plane. The results show that the copepods moved freely in the horizontal plane (x-y plane) and they tended to have faster moving speeds in this plane than in the vertical direction (z axis).

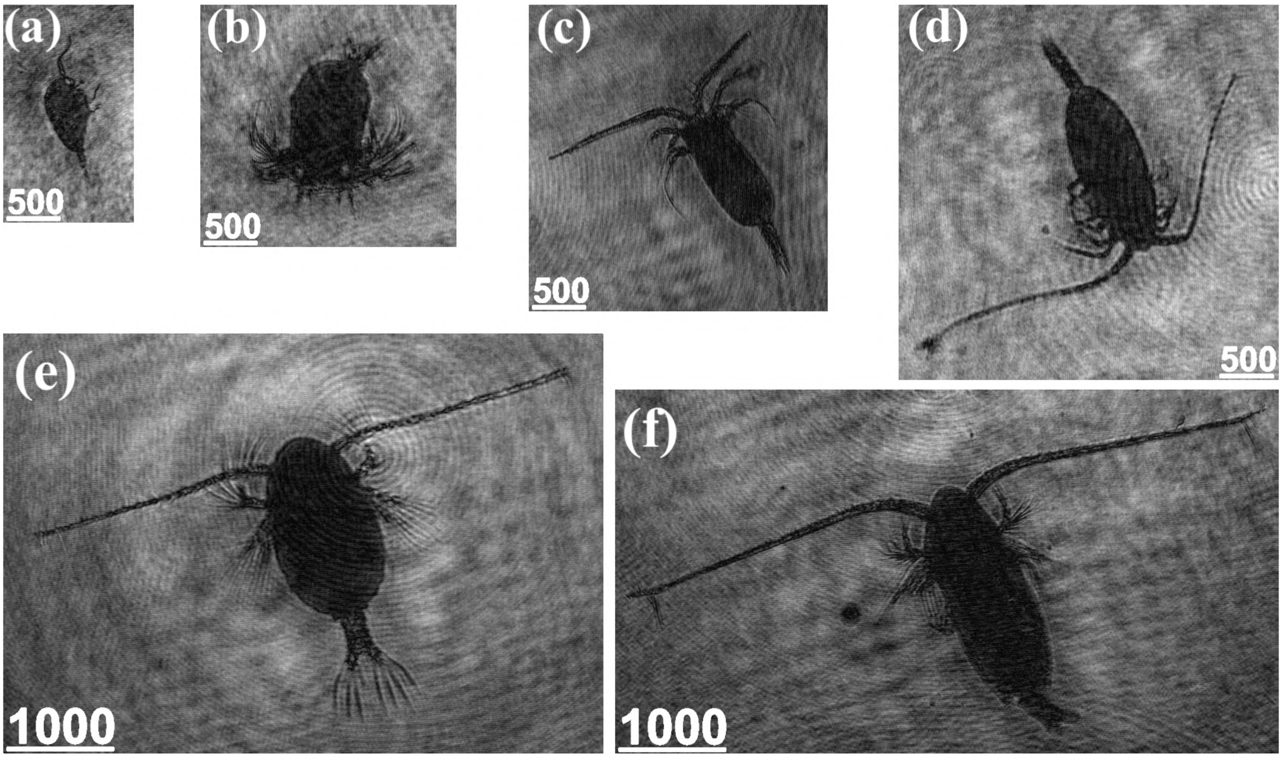

Fig. 16. Reconstructed holograms of six copepods of different size. (a) – Cop1; (b) – Cop2; (c) – Cop3; (d) – Cop4; (e) – Cop5; (f) – Cop6. The unit of scale in the images is µm.

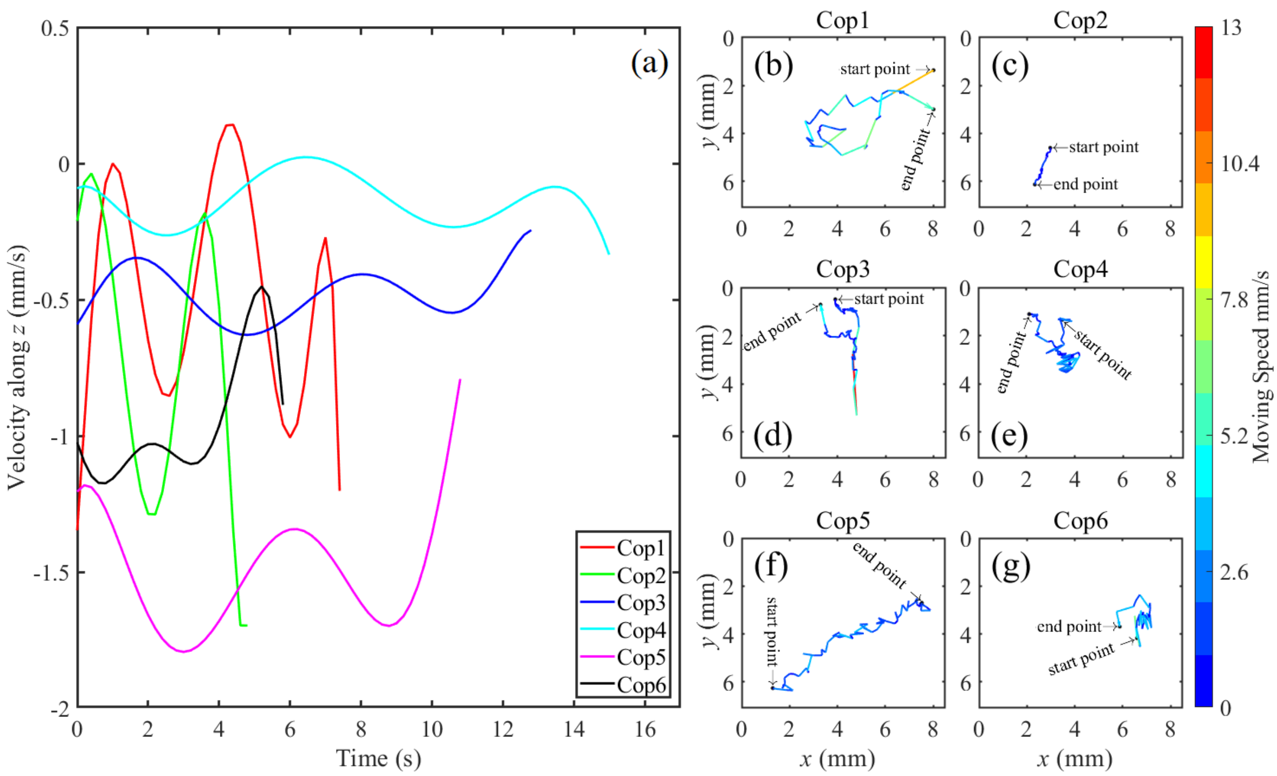

Fig. 17. Comparison of velocities along the z axis (a) and swimming trajectories with moving speeds in the (x, y) plane of six copepods (b)-(g). The curves in (a) are generated using the method of polynomial curve fitting.

TABLE 5. AVERAGE VELOCITIES ALONG THE Z AXIS AND MOVING SPEEDS IN THE (X, Y) PLANE OF SIX COPEPODS

Sample	Cop1	Cop2	Cop3	Cop4	Cop5	Cop6
Average Velocity along z (mm/s)	-0.48	-0.73	-0.48	-0.14	-1.49	-0.95
Average Moving Speed in x-y Plane	2.47	0.54	1.23	1.37	1.65	2.03

5 Conclusions

This work has demonstrated for the first time, multi-centimetre-extent vertical motion tracking of sparsely distributed plankton and other particles at micrometre scale resolution using a novel, compact and low-power, in-line holographic imaging system. The key findings of our experiments are:

- The combination of a CW laser with a short exposure (7 μs at shortest), low parasitic exposure CMOS camera (pixel pitch – 3.45 μm × 3.45 μm) can obtain motion blur free holograms of organic and inorganic particles travelling at up to 490 mm/s in theory. The maximum moving speed of motion blur free tested in experiment is about 200 mm/s. This is sufficient to study the motion of both active and inactive particles found in the ocean, from static or slow-moving sensing platforms. With an in-line holographic measurement setup, we were able to record particles of a size down to ~20 μm over a 20 cm long measurement channel with a 12 mL measurement volume. The simplicity of this setup compared to systems that use pulsed lasers reduces the risk of optical damage to components, increasing system reliability and offers potential size and power reductions. This, combined with the ability to measure large volumes at micron-order resolution, could make the setup more suitable for long-term monitoring of sparsely-distributed deep-sea particles than conventional holographic imaging systems using pulsed lasers.
- The ability to track the vertical motion of a single particle over a several-centimetre range at a micrometre-order resolution could allow differentiation between active, free-swimming organisms such as live plankton, and inactive particles such as inorganic foraminifera shells. The ability to

distinguish particle type is significant when studying vertical transport of carbon and other elements.

- The ability to measure behavioural patterns of active organisms also provides identical features that can be used to facilitate the identification and classification of them at the species level.

Acknowledgements

This work is funded by a joint UK-Japan research program (NERC-JST SICORP Marine Sensor Proof of Concept under project code NE/R01227X/1).

The authors would like to thank the captain, crew, science party and technical support staff of the R/V *Yokosuka* cruise YK20-E02. We also thank Dr. Y. Nagai for providing us the foraminifera samples.

References

[1] GOOS: The Global Ocean Observing System. https://www.goosocean.org (accessed Apr. 29, 2020).

[2] F. Lombard, E. Boss, A. Waite, et al, "Globally consistent quantitative observations of planktonic ecosystems," *Front. Mar. Sci.*, vol. 6:196, Apr. 2019.

[3] A. Gupta, A. Roy, A. Saha, and S. S. Ray, "Flocking of active particles in a turbulent flow," *Phys. Rev. Fluids*, vol. 5, 052601(R), May 2020.

[4] E. Sodré and R. Bozelli, "How planktonic microcrustaceans respond to environment and affect ecosystem: a functional trait perspective," *Int. Aquat. Res.*, vol. 11, pp. 207–223, Jul. 2019.

[5] D. Lindsay, A. Yamaguchi, M. Grossmann, et al, "Vertical profiles of marine particulates: a step towards global scale comparisons using an Autonomous Visual Plankton Recorder," *Bull. Plankton Soc. Japan*, vol. 61, no. 1, pp. 72–81, 2014.

[6] A. Jamieson, L. Brooks, W. Reid, S. Piertney, B. Narayanaswamy, and T. Linley, “Microplastics and synthetic particles ingested by deep-sea amphipods in six of the deepest marine ecosystems on Earth,” *R. Soc. Open Sci.*, vol. 6:180667, Feb. 2019.

[7] S. Giering, E. Cavan, S. Basedow, et al, “Sinking organic particles in the ocean—flux estimates from in situ optical devices,” *Front. Mar. Sci.*, vol. 6:834, Feb. 2020.

[8] E. Malkiel, J. Sheng, J. Katz, and J. Strickler, “The three-dimensional flow field generated by a feeding calanoid copepod measured using digital holography,” *J. Exp. Biol.*, vol. 206, pp. 3657–3666, Jul. 2003.

[9] B. Gemmella, J. Sheng, and E. Buskeya, “Compensatory escape mechanism at low Reynolds number,” *PNAS*, vol. 110, no. 12, pp. 4661–4666, Mar. 2013.

[10] M. Sohn, S. Lim, K. Seo, and S. LEE, “Effect of ambient medium viscosity on the motility and flagella motion of *Prorocentrum minimum* (Dinophyceae),” *J. Plankton Res.*, vol. 35, no. 6, pp. 1294–1304, Jul. 2013.

[11] A. Mullen1, T. Treibitz, P. Roberts, E. Kelly, R. Horwitz, J. Smith, and J. Jaffe, “Underwater microscopy for in situ studies of benthic ecosystems,” *Nat. Commun.*, vol. 7: 12093, Jul. 2016.

[12] J. Song, H. Bib, Z. Cai, X. Cheng, Y. He, M. C. Benfield, and C. Fan, “Early warning of Noctiluca scintillans blooms using in-situ plankton imaging system: An example from Dapeng Bay, P.R. China,” *Ecol. Indic.*, vol 112: 106123, Jan. 2020.

[13] M. Lunven, J. Landeira, M. Lehaître, R. Siano, C. Podeur, and M. Madeleine, “In situ video and fluorescence analysis (VFA) of marine particles: applications to phytoplankton ecological studies,” *Limnol. Oceanogr.: Methods*, vol. 10, pp. 807–823, Oct. 2012.

[14] T. Colomb, N. Pavillon, J. Kühn, E. Cuche, C. Depeursinge, and Y. Emery, “Extended depth-of-focus by digital holographic microscopy,” *Opt. Lett.*, vol. 35, no. 11, pp. 1840–1842, Jun. 2010.

[15] U. Schnars, C. Falldorf, J. Watson, and W. Jüptner, "Digital Holographic Particle Sizing and Microscopy," in *Digital Holography and Wavefront Sensing*, 2th ed. Berlin, Heidelberg, Germany: Springer, 2015, ch. 5, sec. 2, pp. 96–104.

[16] J. Garcia-Sucerquia, W. Xu, S. Jericho, P. Klages, M. Jericho, and H. Kreuzer, "Digital in-line holographic microscopy," *Appl. Opt.*, vol. 45, no. 5, pp. 836–850, Feb. 2006.

[17] J. Flewellen, I. Zaid, and R. Berry, "A multi-mode digital holographic microscope," *Rev. Sci. Instrum.*, vol. 90: 023705, Feb. 2019.

[18] D. Pfitsch, E. Malkiel, Y. Ronzhes, S. King, J. Sheng, and J. Katz, "Development of a free-drifting submersible digital holographic imaging system," in MTS/IEEE Oceans 2005, Washington, DC, USA, Sep. 2005.

[19] S. Talapatra, J. Sullivan, J. Katz, M. Twardowski, H. Czerski, P. Donaghay, J. Hong, R. Jan, M. McFarland, A. Nayak, and C. Zhang, "Application of in-situ digital holography in the study of particles, organisms and bubbles within their natural environment," in Proc. SPIE 8372, Ocean Sensing and Monitoring IV, 837205, Baltimore, Maryland, USA, Jun. 2012.

[20] H. Sun and D. Hendry and M. Player, and John Watson, "In situ underwater electronic holographic camera for studies of plankton," *IEEE J. Ocean. Eng.*, vol. 32, no. 2, pp. 373–382, Apr. 2007.

[21] 4Deep: HoloSea. http://4-deep.com/products/submersible-microscope/ (accessed Apr. 29, 2020).

[22] SEQUOIA: LISST-Holo2. https://www.sequoiasci.com/product/lisst-holo/ (accessed Apr. 29, 2020).

[23] F. Göltenboth, S. Schoppe, and P. Widmann, "Open Ocean," in *Tropical Ecology of Southeast Asia*, F. Goltenboth, K. Timotius, P. Milan, and J. Margraf, Ed. Amsterdam, The Netherlands, Elsevier, 2006, ch. 2, sec. 5, pp. 71–84.

[24] J. Mateos-Perez, R. Redondo, R. Nava, et al, "Comparative evaluation of autofocus algorithms for a real-time system for automatic detection of *Mycobacterium tuberculosis*," *Cytom. Part A*, vol. 81, no. 3, pp. 213–221, Mar. 2012.

[25] T. Yokoyama, M. Tsutsui, M. Suzuki, Y. Nishi, I. Mizuno, and A. Lahav, "Development of low parasitic light sensitivity and low dark current 2.8 μm global shutter pixel," *Sensors*, vol. 18, no. 2: 349, Feb. 2018.

[26] A. Visser, "Motility of zooplankton: fitness, foraging and predation," *J. Plankton Res.*, vol. 29, no. 5, pp. 447–461, May 2007.

[27] C. Borg, E. Bruno, and T. Kiørboe, "The kinematics of swimming and relocation jumps in copepod nauplii," *PLoS ONE*, vol. 7, no. 10: e47486, Oct. 2012.

[28] M. McManus and C. Woodson, "Plankton distribution and ocean dispersal," *J. Exp. Biol.*, vol. 215, pp. 1008–1016, Feb. 2012.

[29] D. Stearns and R. Forward, Jr., "Copepod photobehavior in a simulated natural light environment and its relation to nocturnal vertical migration," *Mar. Biol.*, vol. 82, pp. 91–100, Aug. 1984.

[30] L. Lain and S. Bernard, "The fundamental contribution of phytoplankton spectral scattering to ocean colour: implications for satellite detection of phytoplankton community structure," *Appl. Sci.*, vol. 8, no. 12:2681, Dec. 2018.

[31] G. Graham and W. Nimmo-Smith, "The application of holography to the analysis of size and settling velocity of suspended cohesive sediments," *Limnol. Oceanogr.: Methods*, vol. 8, pp. 1–15, Jan. 2010.

[32] A. Bochdansky, M. Jericho, and G. Herndl, "Development and deployment of a point-source digital inline holographic microscope for the study of plankton and particles to a depth of 6000 m," *Limnol. Oceanogr.: Methods*, vol. 11, pp. 28–40, Jan. 2013.

[33] T. Latychevskaia and H. Fink, "Practical algorithms for simulation and reconstruction of digital in-line holograms," *Appl. Opt.*, vol. 54, no. 9, pp. 2424–2434, Mar. 2015.

[34] J. Mateos-Perez, R. Redondo, R. Nava, et al, "Comparative evaluation of autofocus algorithms for a real-time system for automatic detection of *Mycobacterium tuberculosis*," *Cytom. Part A*, vol. 81, no. 3, pp. 213–221, Mar. 2012.

[35] P. Dollar and C. Zitnick, "Structured forests for fast edge detection," in IEEE Int. Conf. Comput. Vis., pp. 3–8, Sydney, NSW, Australia, Dec. 2013.

[36] K. D. Mielenz, "On the Diffraction Limit for Lensless Imaging," *J. Res. Natl. Inst. Stand. Technol.*, pp. 479–485, vol. 104, no. 479, 1999.

[37] J. van Rooij and J. Kalkman "Axial-resolution in depth from focus digital holography," in Proc. SPIE 10335, Digital Optical Technologies 2017, Munich, Germany, Jun. 2017.

[38] S. Dai and Y. Wu, "Motion from blur," in IEEE Conf. Comput. Vis. Pattern Recogn., Anchorage, USA, Jun. 2008.

[39] B. Pueo, "High speed cameras for motion analysis in sports science," *J. Hum. Sport Exerc.*, vol. 11(1), pp. 53–73, 2016.

[40] Deep Tow (JAMSTEC, Japan). https://www.jamstec.go.jp/e/about/equipment/ships/deeptow.html (accessed Apr. 20, 2020).